Magnetic flux circulation in the Saturnian magnetosphere as constrained by Cassini observations in the inner magnetosphere

Hairong Lai[1], Ying-Dong Jia[2], Christopher T. Russell[2], Xianzhe Jia[3], Adam Masters[4], Michele K. Dougherty[4], Jun Cui[1]

[1] Planetary Environmental and Astrobiological Research Laboratory (PEARL), School of Atmospheric Sciences, Sun Yat-sen University, Zhuhai, Guangdong, China

[2] Department of Earth, Planetary, and Space Sciences, University of California, Los Angeles, CA, USA

[3] University of Michigan, Ann Arbor, MI, USA

[4] Blackett Laboratory, Imperial College London, London, UK

Abstract

In steady state, magnetic flux conservation must be maintained in Saturn's magnetosphere. The Enceladus plumes add mass to magnetic flux tubes in the inner magnetosphere, and centrifugal force pulls the mass-loaded flux tubes outward. Those flux tubes are carried outward to the magnetotail where they deposit their mass and return to the mass loading region. It may take days for the magnetic flux to be carried outward to the tail, but the return of the nearly empty flux tubes can last only several hours, with speeds of inward motion around 200km/s. Using time sequences of Cassini particle count rate, the difference in curvature drift and gradient drift is accounted for to determine the return speed, age and starting dipole L-shell of return flux tubes. Determination of this flux-return process improves our understanding of the magnetic flux circulation at Saturn, and provides insight into how other giant planets remove the mass added by their moons.

1. Introduction

The plasma and magnetic flux circulations in the Saturnian magnetosphere, a fast-rotating system with an inner plasma source [e.g., Burger et al., 2007; Holmberg et al., 2012], are usually considered to be driven intrinsically by the Vasyliunas cycle [Vasyliunas, 1983]. Recently, evidence for a solar wind-driven Dungey cycle [Dungey, 1963] was also found at Saturn [Badman and Cowley, 2007]. In both cycles, the cold plasma stretches the magnetic flux tubes outward, and eventually is allowed to escape from the magnetosphere by reconnection. Meanwhile, conservation of total magnetic flux requires the emptied flux tubes to return to the mass-loading region by buoyancy.

The return magnetic flux is well distinguishable using the Cassini magnetometer and plasma data: Over 700 such events, from 5 to 18 Rs (Rs= 60268 km is Saturn's radius), have been identified and catalogued by Lai et al. [2016]. During these events, in magnetic field strength, such return flux tubes feature intermittent short-duration increase/decrease with abrupt onset and recovery, while in plasma data, cold plasma is depleted, replaced by hot and tenuous plasma. In addition to the radially inward relaxation, these flux tubes may also be diverted azimuthally by the rotating ionosphere [Burch et al., 2005].

Currently, two different types of flux-return processes are proposed: A simple picture expects the empty flux tubes to return directly to the inner magnetosphere, after they are formed in tail reconnection, which usually takes place beyond 20~30Rs [Smith et al., 2016]. As one piece of evidence, the statistical study by Lai et al. [2016] found no boundary from 4 to 18 Rs in the distribution of the flux tube properties. In the other picture, Thomsen et al. [2015] postulated a plasma boundary at around 8.6 Rs using case studies, and more recent statistical results set this boundary at ~10 Rs [Thomsen & Coates, 2019]. They propose that the return flux tubes would stop at the plasma boundary. To penetrate further, an "interchange" process is proposed in their model to swap magnetic flux within this boundary. Empty return flux tubes outside the plasma boundary would interchange with flux tubes loaded with cold plasma inside the plasmasphere. This process has been employed in some

magnetohydrodynamic simulations [e.g., Winglee et al., 2013]. Hence, determination of the starting dipole L shell (L_s) of the return flux tubes is an effective way to distinguish the two different proposed processes.

The history of the return process should be recorded in the hot plasma population inside the return flux tubes until they encounter another significant change in their environment conditions, such as entry into the mass loading region near Enceladus [Jia et al., 2016]. After drifting in the curved magnetic field, higher energy ions arrive earlier at a spacecraft and vice versa for electrons, forming a monotonic curve in their energy spectrum, respectively, as sketched in Figure 2 in Hill et al. [2005]. The authors fitted these slopes linearly, related them to the age of return flux tubes, which are identified from plasma data only, and found most of the flux tubes to be less than 2 hours old [Hill et al., 2005; Chen and Hill, 2008]. Based on the estimated age, whether the injection locations are organized by the Saturnian longitude or local time is still under debate [Hill et al, 2005; Chen and Hill, 2008; Kennelly et al., 2013; Azari et al. 2019].

By assuming conservation of the first adiabatic invariant and introducing a constant radial return speed, Paranicas et al. [2016 and 2020] used a similar method to model the energy dispersion of electrons. However, with an extra unknown variable employed, the radial velocity and L_s have a wide range of solutions. The authors thus compared the measured phase-space density to its background average to obtain L_s and then the radial velocity and age. It is found that a return speed between 0 and 50km/s with an average at 22km/s results in an energy-time dispersion of electrons, which matches observations the best. In addition, the authors also found that for "fresh" events, the age of the observed flux tubes is 1~2hr, and L_s is about 1Rs radially outward from the point of observation, supporting the two-step return theory.

After repeating their work, we further analyzed the difference between gradient drift and curvature drift that depends on the pitch angle of the particles when they pass the equator. We find that even particles in one energy channel of the detectors

should still be drifting at different speeds due to their different pitch angles, as shown in Figure 1, for example. Such a dispersive drift in particles of different pitch angles creates a trapezoid shape in their count rate across the return flux tube, which gives us extra constraint and thus a unique solution.

In this study, we revisit the detailed structures in count rate distributions of ions/electrons at each energy channel available, and fit these structures with our new method that incorporates more physics to determine the return speed u, the L_s and age of the empty flux tubes on detection. The data we used is described in Section 2; model and results are shown in Section 3; and Section 4 concludes this study with a discussion of the results.

2. Data

Three data sets are used in this study: Magnetic field data of one-second resolution measured by the Cassini magnetometer (MAG) [Dougherty et al., 2013], 4-second resolution electron spectrometer (ELS) data (energy range from 0.58eV to 26.04keV) and 16-second resolution ion mass spectrometer (IMS) data (energy range from 1.19eV to 46.34keV) from Cassini plasma spectrometer (CAPS) [Young et al., 2004].

Figure 1 shows the magnetic field and plasma count rate during the same event studied by Paranicas et al. [2016] (this paper is referenced as Paranicas16 hereafter). Since the measurement was obtained on 17 November 2007, we name it the Nov07 event hereafter. Although we use a lower energy dataset, a “straight-back blade” shape similar to Figure 1 in Paranicas16 is shown in the time-energy spectrum of Figure 1. In the panels below, the effect of differential drifting between particles conducting gradient and curvature drifts shows up in each energy channel of the electron count rate: From bottom to top, the shape of the count rate inside the tube transforms gradually from a rectangle for relatively low energy electrons to a trapezoid, and eventually into a triangle for high energy electrons. The trapezoid-shaped profiles are visible from 2.1 keV to 5.4 keV. As an example, a blue triangle

and a red square are added to mark the slanted side along the profile of 4keV electrons. The two points are defined at the two vertices of the best fitted trapezoid (red dashed line), whose two parallel sides are parallel to the x-axis. Both vertices are inside the flux tube, to be consistent with our theory. The final result is found not sensitive to the location of these two points, so some points can be estimated manually. As energy increases, drifting enhances, so the slanted side moves to the right, and the slope decreases, until the 10.1keV energy channel, at which the top spot (red) touches the boundary of the flux tube, leaving a triangular shape in the flux tube. The same evolution of these shapes is found in the ion distribution during other events (not shown). At the boundary of the flux tubes, the sharp changes in magnetic field only affects the counts of electrons with energy below ~700eV (not shown), and thus this effect is not discussed further.

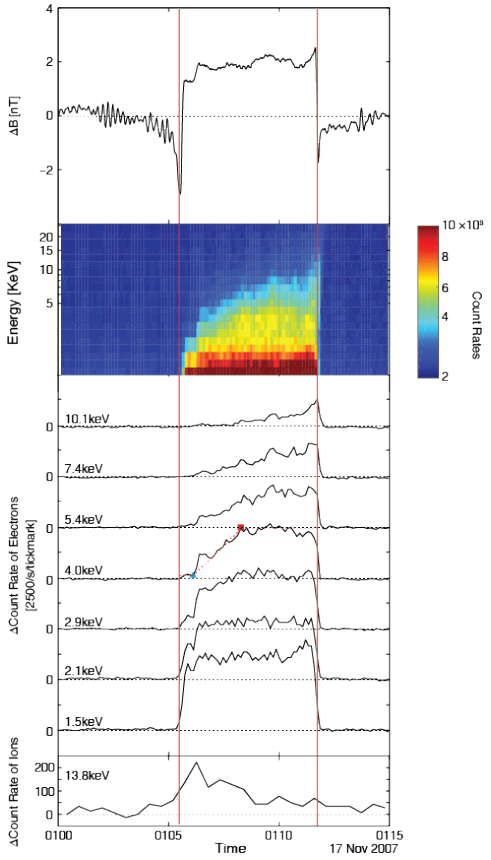

Figure 1. Detrended magnetic field and plasma profiles during the event on 17 November 2007 [Paranicas et al., 2016]. The two vertical red lines mark the boundary of the flux tube that is empty of water group ions and has "floated" inward from the tail. The sinusoidal oscillations in the top panel are ion cyclotron waves induced by water group ions added by the Enceladus plume. This event was detected at a Saturn-centric distance of 5.9Rs, a latitude of 3.19°, and a local time of 21.03 Hours.

3. Model and results

In Paranicas16, only gradient drift is considered, assuming that particles with the same energy drift at the same speed. This is inconsistent with the observed trapezoid-shaped electron counts, which requires multiple drift motions to elongate the returning flux rope. In a curved magnetic field, a charged particle naturally drifts at a speed combining two different mechanisms: Gradient drift V_g and curvature drift V_c:

$$V_g = W_\perp \frac{\mathbf{B}\times\nabla\mathbf{B}}{qB^3},\ V_c = 2W_\parallel \frac{\mathbf{B}\times\nabla\mathbf{B}}{qB^3}, \quad (1)$$

where $W_\perp$ is the energy of the particle thermal velocity component perpendicular to the ambient magnetic field, and $W_\parallel$ is the parallel energy [Kivelson and Russell, 1995].

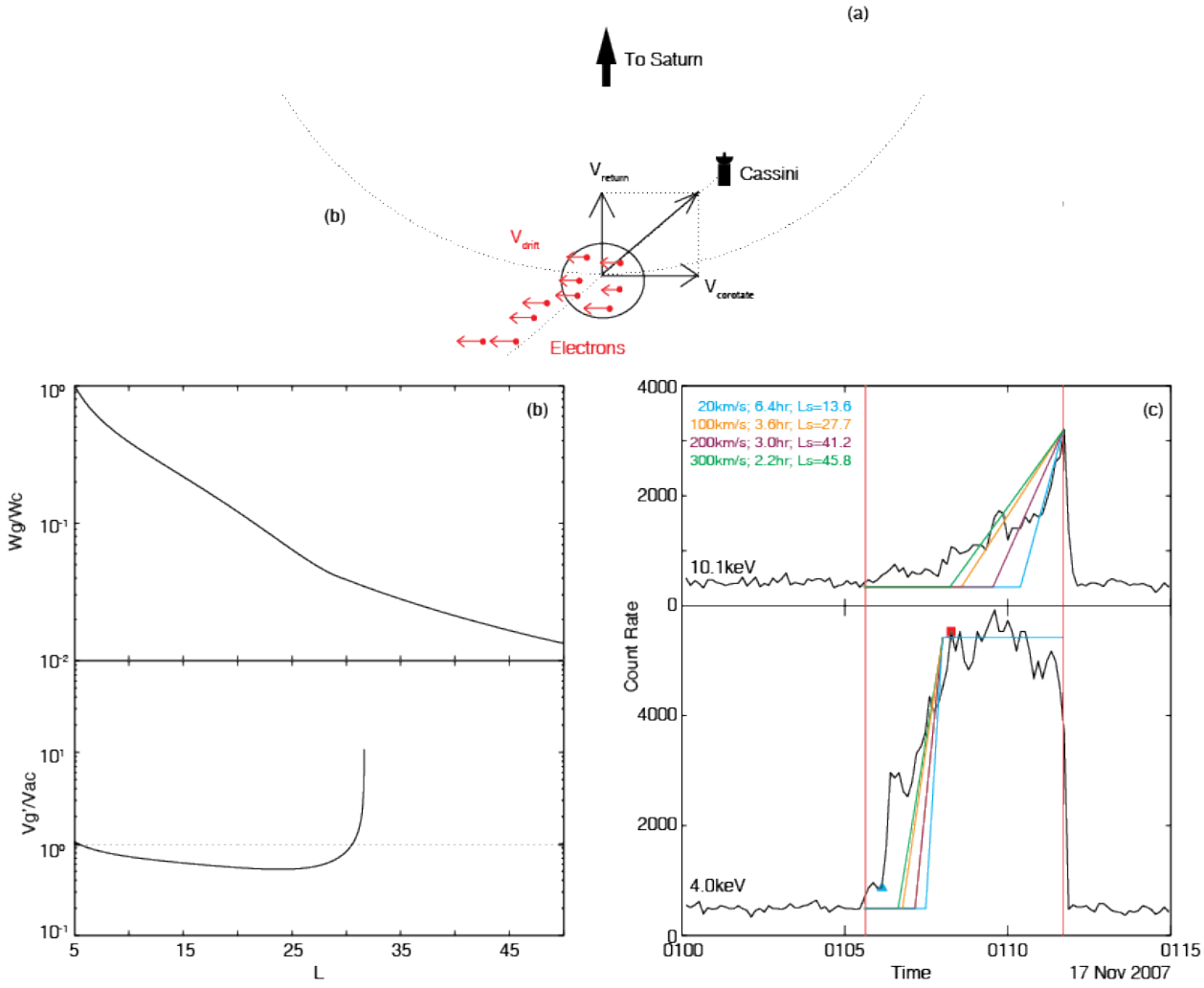

Figure 2. (a) A cartoon illustrating the combination of drift motion of electrons and the return motion of the flux tubes. (b) Comparisons of curvature and gradient drift motions in a stretched magnetosphere: Top panel plots the ratio of the energies related to different drift motions, while bottom panel plots the calculated ratio between drift speeds V_g'/V_{ac}, with the dashed line marking unity. (c) Modeled electron counts at different return speeds, u, of the flux tube (color-coded) compared to the observations: upper panel shows time series for 10.1 keV electrons, while lower panel shows result for 4.0 keV electrons.

In Saturnian magnetosphere, for the electrons, both drifts are in the direction against the corotating plasma. The relative motions of the flux tube and electrons are summarized in Figure 2(a). To determine the return history and match the observed curve of count rate, it is necessary to figure out the leading drift motion, which

depends not only on the corresponding energy, but also on the bouncing process. For a particle with energy $W_{//}=W_{\perp}$, as can be seen from equation (1), its instantaneous curvature drift speed V_c is twice the gradient drift speed V_g at the equator. However, the bounce-averaged "pure" curvature drift speed (V_{ac}) for 0° pitch angle particle is about 0.7 times the "pure" gradient drift for 90° pitch angle in a dipole field [Hamlin et al. 1961].

The real magnetosphere field that returning particles drift in is usually significantly from a dipole field [Kivelson and Russell, 1995].To assess the effect of the stretched field on the drift process, we run a steady-state global magnetohydrodynamic (MHD) simulation of Saturn's magnetosphere using the BATS-R-US code, with 0° magnetic declination [Connerney et al., 1982] and similar mass loading as presented by Jia and Kivelson [2012], but on a coarse Cartesian grid, to generate a set of stretched magnetic field lines stretched by the fast rotating planet (also see Appendix). From observations, the field strength inside the flux tube is about 4.5% increase over the background [Lai et al., 2016]. Therefore, it is safe to use the background field strength and curvature offered by this model in the following calculation.

At L_d, where the event is detected, electrons in the same energy channel are assumed to have the same energy $W(L_d)$. However, when the return process is traced backward, the inferred energy $W(L)$ of those electrons varies depending on their pitch angle $\theta(L)$. In the equatorial plane, the estimated loss cones of particles are less than 10° in this part of the Saturnian magnetosphere, so it is safe to neglect the loss cone effect and investigate a $v = v_{\perp}$, or "perpendicular" (90° pitch angle) case and an approximately $v = v_{\parallel}$, or "perpendicular" (90° pitch angle) case as two extremities. In addition, the calculated flux tube return process where the drifts take place lasts at least several hours, which is much slower than the gyroperiod and bounce periods of electrons of at most several minutes. Therefore, we can assume that the first adiabatic invariant is conserved for "perpendicular" case during its relatively slow gradient

drift, and the second adiabatic invariant is conserved for the "parallel" case during its curvature drift, respectively. With the calculated known field strength and geometry using our magnetospheric MHD model, the variation of "perpendicular"/"parallel" (W_g/W_c) energy as a function of the radial distance is shown in top panel of Figure 2(b): in order to end up with the same energy at L_d, a "parallel" particle needs to start with and always keep at a higher energy: $W_c(L) > W_g(L)$.

To estimate V_{ac}, the bounce averaged curvature drift speed, in the stretched magnetic field, we launch test particles with different pitch angles θ from 0.1° to 85.1° at the equator, with a step size of 5°, at an L shell. For each of such particles *i*, following the procedures in Hamlin et al. [1961], we calculate the coordinates of the pair of mirror points. Between this pair of mirror points, we integrate the angular displacement Φ resulting from both gradient and curvature drift in a bounce period (T_b) to obtain the bounce-averaged angular drift speed $\omega_{ai} = \Phi(\theta_i, L)/T_b(\theta_i, L)$ using equation (1). In addition, to calculate the extreme case of parallel electrons, we then extrapolate the drift speed ratio $R(\theta, L)= \frac{\omega_a(\theta,L)L}{V'_g(L)}$ to θ=0° to obtain R(0°, L) = $\frac{V_{ac}(L)}{V'_g(L)}$. Here V'_g is the averaged gradient drift speed. As an example, at L=5, where the magnetic field is almost dipolar, this ratio is R(0°, 5) = 0.8, close to the 0.7 value in a pure dipole magnetic field [Hamlin et al. 1961].

We repeat such θ extrapolation for each of the integer L between 5 and 40, and the variation of $\frac{V'_g}{V_{ac}}$ ratio as a function of L is shown in the bottom panel of Figure 2(b). Inside ~29Rs, due to the higher energy of the "parallel" particles, V_{ac} is slightly larger than V'_g. However, close to the tail reconnection X-line where the magnetic field lines are highly stretched, the local radius of curvature is huge off the equator, decreasing V_{ac} to almost zero. Therefore, beyond $29R_S$, only perpendicular particles undergo significant gradient drift motions. The ratio $\frac{V'_g}{V_{ac}}$ changes from below to above unity implies that depending on the L_s location, the leading particles in drift

motions can be either parallel or perpendicular ones: If $L_s < 29$, "parallel" particles dominated by curvature drift always drift fastest and would be the first to get out of the flux tube while perpendicular particles drift the slowest and would be the ones closest to the "trailing" boundary; while if L_s is well beyond 34, perpendicular particles will lead the drift. Between the two extreme pitch angles, particles with intermediate pitch angles drift at a speed between V_{ac} and V_g', to form the slope in count rates.

Based on the Magnetosphere Imaging Instrument (MIMI) data set, Paranicas16 defined a critical energy, with which electrons gradient drift a distance just equals the diameter of the flux tube. In our model, when curvature drift is also considered, in addition to the distance where fastest electrons drift (red square in Figure 1), the distance corresponding to slowest electrons (blue triangle in Figure 1) also sets a constraint. In this situation, the L_s and age of the flux tube can be determined without comparing the PSD profile. The Nov07 event is used to illustrate our procedure and the results are shown in Figure 2(c). The duration of this Nov07 event is 363.6s, and an 80% sub-corotating speed gives a diameter of the flux tube of $d_0 = 1.77 \times 10^7$m. First, we assume several different averaged return speeds $u(km/s)$. We then examine the 10.1 keV electrons whose top of the slope reaches the right-hand side boundary, indicating that the faster particles at that energy have drifted entirely out of the flux tube. Two electrons with energy $W_g = 10.1keV$ and $W_c = 10.1keV$ are released at $L_d = 5.9$. A 1-second time step is chosen to trace the electrons backward: at ith second, the two electrons are at $L = L_d + iu/R_s$ with drifting speed $V_g'(L)$ and $V_{ac}(L)$, respectively. This tracing process stops when the faster electron has crossed the distance of d_0 and the corresponding travel time T is then the age of the flux tube and $L_s = L_e + uT$. For each travel time T, the drift distance d of the slower particles can also be integrated. The results are compared in Figure 2(c): with $200km/s$ and $300km/s$ injection speeds and L_s beyond 40, the top of the slope corresponds to the gradient drift (perpendicular particles), while the

236 bottom of the slope corresponds to the curvature drift (parallel particles). In
237 comparison, with $20\mathrm{km/s}$ and $100\mathrm{km/s}$ injection speeds and L_s inside 29,
238 parallel particles with curvature drift move faster. The best fit is defined as the
239 shortest distance to both the fastest moving point (red square in Figure 1) and the
240 slowest one (blue triangle in Figure 1). In the Nov07 case, a $300\mathrm{km/s}$ injection
241 speed with a $L_s = 45.8$ and travel time $T = 2.2\mathrm{hr}$ returns the best fit. It should be
242 noted that for simplification, the slope as a straight line is a special case of the count
243 curve, which relies on the initial pitch angle distribution of the particles.

244 Two more events detected near equator with well-defined slopes are studied, as
245 shown in Figure 3. The best fit is obtained with an injection speed of $150\mathrm{km/s}$ and
246 $300\mathrm{km/s}$, respectively. In both cases, the perpendicular particles under gradient drift
247 move faster than the parallel ones. Figure 3(a) is, again, the Nov07 event, with all
248 energy channels modeled. As shown, all profiles can be fitted well with a constant
249 velocity.

250 During the returning process of these flux tubes, the evolution of their plasma
251 contents should disturb the magnetic field. Hence, Lai et al. [2016] have identified the
252 flux tubes with “well defined” magnetic field signature as younger events. Compared
253 with the remaining 700 such events, the magnetic field profile during this Nov07
254 event is among the most well-defined [Paranicas et al., 2016], indicating a younger
255 flux tube by the above standard. In this study, our calculated travel time, T, shows that
256 it is the youngest among the three events shown in Figure 3, consistent with the age
257 predictions by Lai et al. [2016]. On the other hand, the case in Figure 3(b) is judged to
258 be “old” from the magnetic field data [Lai et al., 2016], and its modeled travel time is
259 also the longest in this study. Such consistency obtained with two independent
260 methods studying two different data sets strongly supports our picture of particle drift
261 during the flux return processes. We note that the case in Figure 3(c) lasts only 1
262 minute, and the ion data are not shown due to their time resolution of 32 seconds
263 being too low to judge the degree of fitting with our model.

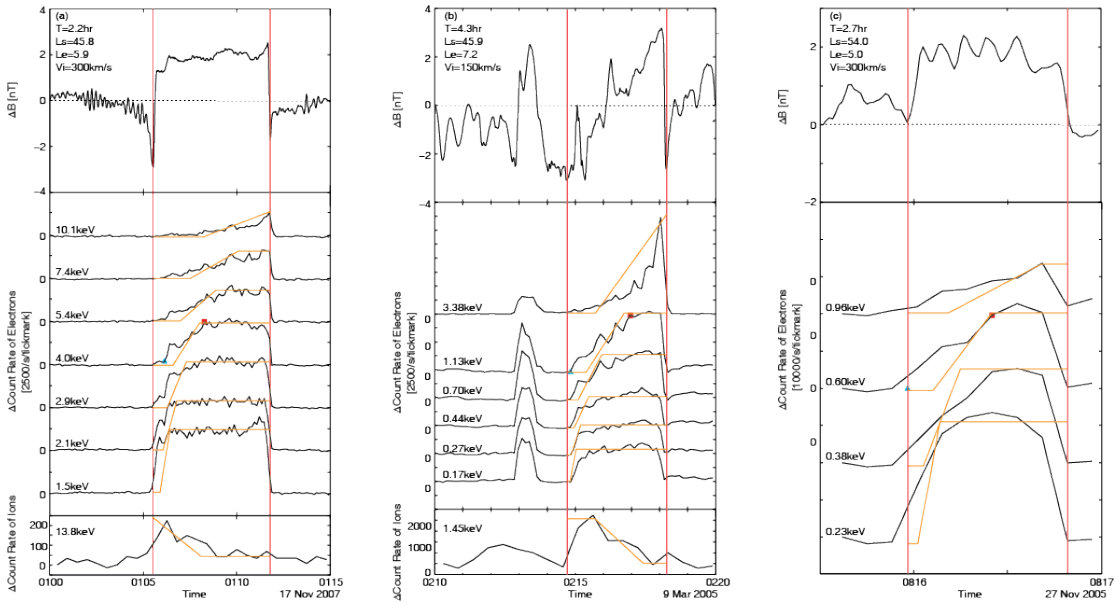

Figure 3. Comparisons of modeled distributions of electrons and ions against Cassini measurements during three flux tube events. All orange lines are modeled by assuming a constant return speed varies from 150km/s to 300km/s.

4. Discussion and conclusions

The Nov07 event was previously studied by Paranicas16, considering an upper cutoff energy (defined as the energy with which electrons can drift out of the flux tube completely) of 60keV and a return speed of $u = 18\text{km/s}$. With only the gradient drift considered, the starting L-shell and travel time are found to be $L_s = 7.2$ and $T = 1.2\text{hr}$, respectively. In addition, the 9 March 2005 event shown in Figure 3(b) has also been studied in Paranicas16, to arrive at an upper cutoff energy at 27keV and return speed of $u = 18\text{km/s}$; a starting L shell of $L_s = 8.55$; and a travel time of $T = 1.3\text{hr}$.

We note that the method adopted by Paranicas16 to fit the whole energy spectrum may bring in a large uncertainty above or below their line fit. Depending on the chosen dataset and the range of color code, the determined upper cutoff energy can be six times smaller (second panel in Figure 1). This artificial bias can be excluded if the count curves are employed as proceeded in our model. Here, with both drifts considered, fits the count curve of relatively lower energy particles (<~10keV)

283 and returns a set of much larger L_s and longer travel times. Another major difference
284 is that Paranicas16 method only calculated the gradient drift but use that drift distance
285 to fit the counterpart of the blue triangle in Figure 1, which is turned out to be
286 completed by curvature drift, as determined with our method. In addition, the data that
287 we use are at the lower end of the energy spectrum and consist of higher counts,
288 associated with lower statistical errors.

289 We acknowledge our significant difference in both method and result with
290 Paranicas16. Their L_s is determined by matching the phase space density (PSD) of
291 the particles inside the injection with the radial profile of the nominal phase space
292 density. We note that there are two over-simplifications in Paranicas16's assumption:
293 First, in their Figure 4, the PSD line is assumed to grow monotonically with L.
294 However, this is inconsistent with the figure. In the same figure, the slope of the
295 averaged PSD line decreases toward 0 as L increases. Hence, we conclude that with
296 Paranicas16's analysis, greater L origin of the flux tubes are inherently excluded with
297 this method. Second, at the location of detection in the inner magnetosphere,
298 including the range of L shells plotted in their Figure 4, the background plasma
299 surrounding the flux tubes is magnetospheric plasma constituting the plasma torus. In
300 contrast, as stated by Hill [2016], the plasma inside the returning flux tube is probably
301 the planetward exhaust from tail reconnection, which should be the entrance of
302 external plasma [Vasyliunas 1983]. There is no reason for the PSD of the torus
303 plasma to match the PSD of solar wind plasma: Searching for a matched PSD of a
304 stream of particles from an external source in the averaged PSD of Saturn's torus
305 particles may not return where the external particles are launched. Therefore, we
306 conclude that what Paranicas16 have found is not necessarily the L_s of flux tube
307 origin. Instead, our method does not have these problems.

308 Our high return velocity from 150km/s to 300km/s is reasonable, as Lai et al.
309 [2016] find that the return speed of flux tubes should be about 200km/s at L=10, and
310 can be up to 80km/s at L=5 by balancing the reconnection rate with the return
311 magnetic flux.

As Figure 2(b) shows, the ratio of perpendicular to parallel energy at the equator varies with L. Therefore, the pitch angle distributions at L_d does not necessary resemble their original pitch angle and energy at L_s, which are not available in any observations. We did not follow a full pitch angle range of particles from L_s to L_d in a particular flux tube. Instead we only use the two extreme points of the curve to determine L_s, as particles of close- to-0° pitch angle and 90° pitch angle at the equator will retain the same drift angle at the same latitude, unless disturbed in a non-adiabatic process. On the other hand, the count of these two extreme types of particles defines the two ends of the line fit, and thus can be compared with the modeled results directly using our method, without requiring the shape of the curve in between, or the unconstrained pitch angle distribution at L_s.

Due to the fluctuations and the time-resolution of the data, the two points on the curve of count rate cannot be determined unambiguously. However, as we can see in Figure 2(c), even a slow return speed gives a L_s beyond 10, which is the key conclusion of this study. This is also true in the other two cases. Therefore, our method is not sensitive to the exact location of the two extreme points.

All starting L shells Ls that we found are greater than 45, when we use the stretched dipole field. This Ls location is way outside the plasmapause. Rather, all our Ls values are consistent with a direct release from the tail reconnection region. Although the magnetospheres of the gas giants are largely internally driven, the solar wind plays a major role in shaping the magnetic field in distant regions away from the planets [e.g., Arridge et al., 2008]. However, because age $T = R_s \int \frac{dL}{u}$, the relatively slower travel speed in the inner magnetosphere where the field is less influenced by the solar wind contributes more to the total age, so even if there is a warped dynamic magnetotail different from out stretched dipole, we will still arrive at L_s is not in the inner magnetosphere, but close to the tail reconnection site. Similarly, in the Jovian magnetosphere, the non-axisymmetry of the internal field relative to the rotation axis [Russell and Dougherty, 2010 and references therein] is expected to make the

geometry more complicated, but this key conclusion of direct return will not change qualitatively. On the other hand, since the return process consists of a segment in the mid tail, estimating the local time of release at L_s still faces uncertainties and will not be discussed here.

In our simplified model, to figure out the leading drift motion, we use extrapolated results of "pure" parallel particles. The existence of a finite loss cone limits the real curvature drift to be slower than that of the "pure" parallel extremity. However, in the region where L_s locates, the faster particles are under gradient drift motion as shown in Figure 2(c). Therefore, our conclusion of direct return still holds.

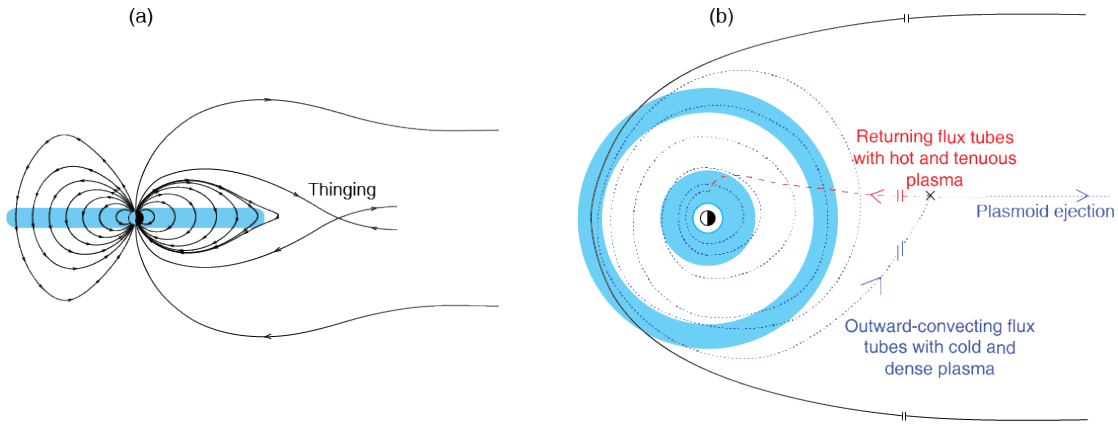

Figure 4. Illustration of the time-integrated circulation of magnetic flux in the Saturnian magnetosphere, indicated by our result. The blue ring is the neutral torus from Enceladus. (a) Black lines are magnetic field lines drawn until around the tail reconnection site in side view. (b) The black line marks the magnetopause. The blue dotted curve sketches the radially slow convection of plasma-loaded magnetic flux tubes spinning outward into the tail. The red dashed line indicates the return of plasma-depleted magnetic field tubes directly back to the inner magnetosphere at a higher radial speed. This red line may not end at the dawn side, but is not expected to wind multiple circles as indicated by the age estimation.

We have applied our model to another 10 cases with both magnetic field and plasma data available. Their starting locations are all found to be Ls >> 10. This result

supports the hypothesis that empty flux tubes generated by reconnection in the far-tail region return directly into the inner magnetosphere. On the other hand, we suspect that even if there is a plasma boundary at around $10R_S$, the effective viscosity may not be sufficient to perturb the return motion significantly. Slowing-down of the returning flux tubes is expected only when mass-loading processes become significant, i.e., inside $6R_S$. A cartoon summarizing our interpreted circulation of magnetic flux in the Saturnian magnetosphere is shown in Figure 4. On the other hand, however, a lot of events studied by Thomsen et al. [2015] and Thomsen and Coates [2019] are not selected based on their magnetic signatures like we did, but on their plasma signatures (second panel in Figure 1), and, therefore, are not included in our study. This different data pool may be a reason for our different conclusions. We leave such distinction to future studies with a new criterion that may accommodate all available data.

In summary, we present case studies to model the fine structures in the particle profiles observed by Cassini during its flux tube encounters. Our new method not only incorporates more physics, but also yields results that are consistent with both the age judged by magnetic measurements, and the velocity estimated by outflow speed. More sophisticated models of magnetic field and plasma background, including numerical simulations, should be applied to improve the accuracy of such studies. Last, the method and understandings we applied to Saturn's magnetosphere should also be applicable to observations of the Jovian magnetosphere obtained by Galileo [Kivelson et al., 1997], Juno [Haggerty et al., 2019], and future missions to the Jupiter system, to determine the circulation of plasma and magnetic flux. For the ice giant planets and exoplanets with limited or no in situ observations available, we believe that such a process may be the best paradigm for global circulation estimates.

Acknowledgments

We would like to acknowledge the Strategic Priority Research Program of Chinese Academy of Science in undertaking this study (Grant Number:

XDB41000000) and the National Natural Science Foundation of China (Grant No. 42074209).

The Cassini data used in this study are available online through NASA PDS (with DOI number 10.17189/1519593 and 10.17189/1519603).

The return flux tube events are chosen from the list in Lai et al. [2016].

References

Arridge, C. S., C. T. Russell, K. K. Khurana, N. Achilleos, S. W. H. Cowley, M. K. Dougherty, D. J. Southwood, and E. J. Bunce (2008), Saturn's magnetodisc current sheet, J. Geophys. Res., 113, A04214, doi:10.1029/2007JA012540.

Azari, A.R., X. Jia, M.W. Liemohn, G.B. Hospodarsky, G. Provan, S.-Y. Ye, S.W.H. Cowley, C. Paranicas, N. Sergis, A.M. Rymer, M.F. Thomsen, and D.G. Mitchell (2019), Are Saturn's interchange injections organized by rotational longitude? Journal of Geophysical Research: Space Physics, 124, 1806–1822. https://doi.org/10.1029/2018JA026196

Badman, S.V. and S.W.H. Cowley (2007), Significance of Dungey-cycle flows in Jupiter's and Saturn's magnetospheres, and their identification on closed equatorial field lines, Ann. Geophys., 25, 941-951.

Burch, J.L., J. Goldstein, T.W. Hill, D.T. Young, F.J. Crary, A.J. Coates, N. André, W.S. Kurth, and E.C. Sittler Jr. (2005), Properties of local plasma injections in Saturn's magnetosphere, Geophys. Res. Lett., 32, L14S02, doi:10.1029/2005GL022611.

Burger, J.L., J. Goldstein, W.S. Lewis, D.T. Young, A.J. Coates, M.K. Dougherty, and N. Andre (2007), Tethys and Dione: Sources of outward flowing plasma in Saturn's magnetosphere, Nature, 447, 833-835, doi:10.1038/nature05906.

412 Chen, Y., and T. W. Hill (2008), Statistical analysis of injection/dispersion events in
413 Saturn's inner magnetosphere, J. Geophys. Res., 113, A07215,
414 doi:10.1029/2008JA013166.

415 Connerney, J., N. Ness, M. Acuna (1982), Zonal harmonic model of Saturn's magnetic
416 field from Voyager 1 and 2 observations, Nature, 298 (1982), pp. 44-46

417 Dougherty, M.K., S. Kellock, A.P. Slootweg, N. Achilleos, S.P. Joy, and J.N. Mafi
418 (2013), CASSINI ORBITER MAG CALIBRATED SUMMARY 1 SEC AVERAGES
419 V1.0, CO-E/SW/J/S-MAG-4-SUMM-1SECAVG-V1.0, NASA Planetary Data
420 System.

421 Dungey, J.W. (1963), The structure of the exosphere or adventures in velocity space.
422 In: De Witt, C., Heiblot, J., Le Beau, L. (Eds.), Geophysics, The Earth's Environment,
423 p. 503.

424 Haggerty, D. K., Mauk, B. H., Paranicas, C. P., Clark, G., Kollmann, P., Rymer, A.
425 M., et al. (2019). Jovian injections observed at high latitude. Geophysical Research
426 Letters, 46, 9397–9404. https://doi.org/10.1029/2019GL083442

427 Hamlin, D. A., R. Karplus, R.C. Vik, and K.M. Watson (1961), Mirror and azimuthal
428 drift frequencies for geomagnetically trapped particles, J. Geophys. Res., 66,1,1-4,
429 doi: 10.1029/JZ066i001p00001.

430 Hill, T.W., A.M. Rymer, J.L. Burch, F.J. Crary, D.T. Young, M.F. Thomsen, D.
431 Delapp, N. Andre´, A.J. Coates, and G.R. Lewis (2005), Evidence for rotationally
432 driven plasma transport in Saturn's magnetosphere, Geophys. Res. Lett., 32, L14S10,
433 doi:10.1029/2005GL022620.

434 Hill, T.W. (2016), Penetration of external plasma into a rotation-driven
435 magnetosphere, J. Geophys. Res. Space Physics, 121, 10,032–10,036,
436 doi:10.1002/2016JA023430.

437 Holmberg, M.K. G., J.-E. Wahlund, M.W. Morooka, and A.M. Persoon (2012), Ion
438 densities and velocities in the inner plasma torus of Saturn, Planet. Space Sci., 73,
439 151–160.

440 Jia, X., and M. G. Kivelson (2012), Driving Saturn's magnetospheric periodicities
441 from the upper atmosphere/ionosphere: Magnetotail response to dual sources, J.
442 Geophys. Res., 117, A11219, doi:10.1029/2012JA018183.

443 Jia, X. Z, M.G. Kivelson, T.I. Gombosi (2016). Global MHD modeling of the coupled
444 magnetosphere-ionosphere system at Saturn, American geophysical union (AGU),
445 chap 25. https://doi.org/10.1002/9781119066880.ch25

446 Kennelly, T. J., J. S. Leisner, G. B. Hospodarsky, and D. A. Gurnett (2013), Ordering
447 of injection events within Saturnian SLS longitude and local time, J. Geophys. Res.
448 Space Physics, 118, 832–838, doi:10.1002/jgra.50152.

449 Kivelson, M. G., & Russell, C. T. (1995). Introduction to Space Physics. New York,
450 USA: Cambridge University Press.

451 Kivelson, M. G., Khurana, K. K., Russell, C. T., & Walker, R. J. (1997). Intermittent
452 short-duration magnetic field anomalies in the Io torus: Evidence for plasma
453 interchange? Geophysical Research Letters, 24, 2127–2130.

454 Lai, H.R., C.T. Russell, Y.D. Jia, H.Y. Wei, and M.K. Dougherty (2016), Transport of
455 magnetic flux and mass in Saturn's inner magnetosphere, J. Geophys. Res. Space
456 Physics, 121, doi:10.1002/2016JA022436.

457 Paranicas, C., M.F. Thomsen, B. Achilleos, M. Andriopoulou, S.V. Badman, G.
458 Hospodarsky, C.M. Jackman, X. Jia, T. Kennelly, K. Khurana, P. Kollmann, N.
459 Krupp, P. Louarn, E. Roussos, and N. Sergis (2016), Effects of radial motion on
460 interchange injections at Saturn, Icarus, 264, 342-351.

461 Paranicas, C., M.F. Thomsen, P. Kollmann, A.R. Azari, A. Bader, S.V. Badman, M.
462 Dumont, J. Kinrade, N. Krupp, and E. Roussos (2020). Inflow speed analysis of

463 interchange injections in Saturn's magnetosphere. Journal of Geophysical Research:
464 Space Physics, 125, e2020JA028299. https://doi.org/10.1029/2020JA028299.

465 Russell, C.T., M.K. Dougherty (2010). Magnetic fields of the outer planets Space Sci.
466 Rev., 152, doi: 10.1007/s11214-009-9621-7

467 Smith, A. W., C. M. Jackman, and M. F. Thomsen (2016), Magnetic reconnection in
468 Saturn's magnetotail: A comprehensive magnetic field survey, J. Geophys. Res. Space
469 Physics, 121, 2984–3005, doi:10.1002/2015JA022005.

470 Thomsen, M.F., D.G. Mitchell, X. Jia, C.M. Jackman, G. Hospodarsky, and A.J.
471 Coates (2015), Plasmapause formation at Saturn, J. Geophys. Res. Space Physics,
472 120, 2571–2583, doi:10.1002/2015JA021008.

473 Thomsen, M. F., & Coates, A. J. (2019), Saturn's plasmapause: Signature of
474 magnetospheric dynamics. Journal of Geophysical Research: Space Physics, 124,
475 8804–8813. https://doi.org/10.1029/2019JA027075.

476 Tóth, G., van der Holst, B., Sokolov, I. V., De Zeeuw, D. L., Gombosi, T. I., Fang, F.,
477 Manchester, W. B.;,Meng, X., Najib, D., Powell, K. G., Stout, Q. F., Glocer, A., Ma,
478 Y.J., & Opher, M. (2012), Adaptive numerical algorithms in space weather modeling,
479 J. Comp. Phys., 231(3), 870-903. doi:10.1016/j.jcp.2011.02.006

480 Vasyliunas, V.M. (1983), Plasma distribution and flow, in: Physics of the Jovian
481 Magnetospehre, edited by: Dessler, A.J., Cambridge Univ. Press, Cambridge, UK,
482 395-453.

483 Winglee, R.M., A. Kidder, E. Harnett, N. Ifland, C. Paty, and D. Snowden (2013),
484 Generation of periodic signatures at Saturn through Titan's interaction with the
485 centrifugal interchange instability, J. Geophys. Res. Space Physics, 118, 4253–4269,
486 doi:10.1002/jgra.50397.

Young, D. T., Berthelier, J. J., Blanc, M., Burch, J. L., Coates, A. J., Goldstein, R., et al. (2004). Cassini plasma spectrometer investigation. Space Science Reviews, 114(1-4), 1–112. https://doi.org/10.1007/s11214-004-1406-4.

Appendix: The Saturn model that generates the stretched field lines

The following MHD equations are used in this model:

$$\frac{\partial \rho}{\partial t} + \nabla \cdot (\rho \mathbf{u}) = \rho_s \quad \text{(A1)}$$

$$\rho \frac{\partial \mathbf{u}}{\partial t} + \rho(\mathbf{u} \cdot \nabla)\mathbf{u} = -\nabla P - en(\mathbf{u} \times \mathbf{B}) + \mathbf{M_s} \quad \text{(A2)}$$

$$\frac{\partial P}{\partial t} + (\mathbf{u} \cdot \nabla)P + \gamma P(\nabla \cdot \mathbf{u}) = E_s \quad \text{(A3)}$$

$$\frac{\partial \mathbf{B}}{\partial t} = \nabla \times (\mathbf{u} \times \mathbf{B}) \quad \text{(A4)}$$

where e is the electric charge on an electron; ρ, $\mathbf{u}$, and P is the mass density, bulk velocity vector and thermal pressure of the plasma, respectively. Variable $n = \rho/m$ is the number density of protons, m is proton mass, and we neglect the electron momentum. $\mathbf{B}$ is the magnetic field vector, and the mass, momentum, and energy source terms (ρ_s, $\mathbf{M}_s$, E_s) follow the same used by Jia et al. [2012].

Equations (A1-A4) are solved numerically using the Michigan BATS-R-US code [Tóth et al., 2012], on a 204.8×102.4×102.4Rs Cartesian grid, with finest resolution 0.1Rs. A steady state solution is reached, with the following solar wind conditions launched at the $x = 51.2$ Rs upstream boundary: $n = 0.0081/cc$, $T = 10^4 K$, $U = U_x = 615 km/s$, $\mathbf{B} = (0.00594, 0.00173, 0.00063) nT$. Saturn's dipole tilt is assumed to be 0. Ionospheric inner boundary is assumed at $r = 3.5$Rs, where thermal pressure and magnetic field has 0 gradient (float), plasma velocity is 0 at the inner boundary interface, and density is set to constant $n_{in} = 70/cc$.